Zebrafish otic vesicle and mouse epididymis as model systems for studying columnar epithelial cell division

Yu Xia[1,2,*], Björn Perder[1,2,*], Alvin Gea Chen Yao[1,2], Miaoyan Qiu[1,2], Jingli Cao[1,2,#]

[1]Cardiovascular Research Institute, Weill Cornell Medicine, 1300 York Avenue, New York, NY, USA

[2]Department of Cell and Developmental Biology, Weill Cornell Medicine, 1300 York Avenue, New York, NY, USA

[#]Correspondence: Jingli Cao, jic4001@med.cornell.edu

*These authors contributed equally.

Running title: Epithelial cell division in otic vesicle and epididymis

Key words: epithelial cell division, interkinetic nuclear migration, zebrafish otic vesicle, mouse epididymis, live imaging

ABSTRACT

Epithelial cell division maintains tissue architecture through coordinated nuclear migration, cell shape changes, and spindle orientation. In columnar epithelia, interkinetic nuclear migration (INM) involves apical nuclear translocation in G2 and basal return post-mitosis, yet its regulation and physiological significance remain understudied due to limited live imaging *in vivo* models. We adapted the zebrafish embryonic otic vesicle as an *in vivo* model to study epithelial division dynamics using high-resolution live imaging and genetic tools. We find that apical INM initiates in mid-to-late G2 and is driven by dynein, not myosin II. Mitotic rounding is achieved via actomyosin-mediated basolateral constriction while maintaining basal attachment. Inhibiting myosin II impairs rounding and planar division, causing apical retention of daughter cells, suggesting planar division ensures proper integration. We extend our analysis to the mouse epididymis epithelium, comparing nuclear migration, cell shape, and spindle orientation across species. Our work introduces optimized *in vivo* models and reveals conserved and tissue-specific mechanisms maintaining structure and function of columnar epithelia.

INTRODUCTION

Epithelial cell division is a tightly regulated process that preserves tissue architecture and function by coordinating cell shape changes, polarity maintenance, and spindle orientation. A defining feature of epithelial tissues is their apical-basal polarity, which is crucial for barrier function, directional transport, and homeostasis (Rodriguez-Boulan and Macara, 2014). Apical membranes form tissue lumens, basal membranes adhere to the basal lamina, and lateral membranes connect neighboring cells through tight and adherens junctions. During mitosis, epithelial cells undergo morphological remodeling while maintaining tissue integrity through dynamic rearrangements of cortical actin and cell junctions. Proper spindle orientation ensures that daughter cells integrate correctly into the epithelium, preventing disruptions that can lead to developmental defects and disease (Morin and Bellaiche, 2011; Godard and Heisenberg, 2019).

Columnar epithelium can be categorized into pseudostratified and simple columnar epithelium. In simple columnar epithelium, such as that in the stomach, intestine, airway epithelia, otic vesicle, epididymis, and prostate, cells are column-shaped with nuclei positioned near the basal lamina (Fujita, 1960; Lee et al., 1994; Tsue et al., 1994; Robaire and Hinton, 2002; Fleming et al., 2007; Bagley et al., 2024). In contrast, pseudostratified epithelium, such as neuroepithelium, exhibits a “pearl-on-a-string” morphology, where cells have thin apical and basal processes, and their nuclei appear multilayered (Baye and Link, 2008; Taverna and Huttner, 2010). A key feature of these columnar epithelia is interkinetic nuclear migration (INM)—nuclear movement toward the apical surface in G2 phase and back to the basal side post-mitosis (Sauer, 1935; Fujita, 1960; Fujita, 1962; Baye and Link, 2008; Taverna and Huttner, 2010). Additionally, cells in these tissues undergo division in specific orientations, typically parallel to the apical membrane, due to polarized mitotic spindle orientation (Fujita, 1960; Ahringer, 2003; Baye and Link, 2008; Taverna and Huttner, 2010; Nakajima et al., 2019). Most mechanistic studies on INM focus on stem or progenitor cells in the neuroepithelium of developing retina or neural

tube. Both microtubules (MTs) and filamentous actin (F-actin) are generally believed to be critical for INM (Baye and Link, 2008; Taverna and Huttner, 2010; Kosodo, 2012). Discrepancies, however, exist, concerning the actual contributions of each cytoskeletal element, possibly due to differences in experimental systems or methods. In rodent neuroepithelia, cytoplasmic dynein, a MT-bonded minus end-directed motor protein, facilitates basal-to-apical nuclear movement, supported by apically anchored centrosomes and nuclear tethering proteins (Gambello et al., 2003; Xie et al., 2007; Zhang et al., 2009; Ge et al., 2010; Taverna and Huttner, 2010; Tsai et al., 2010). Kinesin-3, a MT-bonded plus end-directed motor, drives apical-to-basal movement, while myosin II appears dispensable (Tsai et al., 2010). However, some studies suggest a critical role for myosin II in apical-to-basal migration (Schenk et al., 2009). In zebrafish retina, INM in both directions depends mainly on myosin II (Norden et al., 2009).

In pseudostratified epithelia like neuroepithelium, nuclei navigate through narrow cellular processes (Baye and Link, 2008; Taverna and Huttner, 2010; Kosodo, 2012), whereas in simple columnar epithelia, nuclear migration in G2 may be less constrained, but mitotic rounding requires cytoplasmic displacement toward the apical side. Thus, while INM and division share core mechanisms across epithelial subtypes, distinct structural constraints may influence their regulation. Recent studies analyzing fixed *in vivo* samples and live imaging studies in intestinal organoids and chicken neural tube slices have provided new insights into epithelial division (Spear and Erickson, 2012; Carroll et al., 2017; Saleh et al., 2023). However, key knowledge gaps persist, particularly in how cells integrate mechanical and biochemical cues to drive nuclear migration and position the mitotic spindle, orient division, and maintain tissue integrity. *In vitro* models often fail to capture the complexity of *in vivo* epithelial division, emphasizing the need for physiologically relevant systems of columnar epithelia. Although *in vivo* live imaging has been widely applied to study epithelial cell division in various systems, including mouse skin, zebrafish embryos, and the Drosophila wing disc (e.g., (Campinho et al., 2013;

Bergstralh et al., 2016; Ipponjima et al., 2016; Moore et al., 2023; Xin et al., 2024)), columnar epithelia remain comparatively underexplored in live contexts.

Building on previous work by the Megason group and others (Megason, 2009; Hoijman et al., 2015; Mosaliganti et al., 2019), we adapted the zebrafish embryonic otic vesicle as an optimized *in vivo* model for studying columnar epithelial cell division dynamics, an area that has not been explored in this context, to address the questions outlined above. The zebrafish otic vesicle epithelium offers several advantages, including optical accessibility for high-resolution live imaging and genetic tractability, making it an ideal system for visualizing columnar epithelial cell division in its native context. We also validated some of our findings in the mouse epididymis model, revealing conserved cellular mechanisms underlying epithelial cell division.

RESULTS

INM in zebrafish otic vesicle epithelium begins in late G2

To investigate nuclear behavior during cell division in zebrafish otic vesicle epithelium, we labeled nuclei with H2B-GFP and cell membranes with RFP-F (Hancock et al., 1991; Aronheim et al., 1994) by microinjecting *in vitro*-transcribed mRNAs into fertilized zebrafish eggs. We focused on the ventral side of the otic vesicle, where epithelial cells maintain a tall columnar shape between 22 and 28 hpf (Fig. 1A, B). As expected, while most nuclei remained at the basal side, occasional INM events interspersed with mitosis were observed (Fig. 1C; Videos S1 and S2). The entire migration cycle lasted an average of 70.4 ± 7.7 minutes (n = 10).

We then analyzed nuclear dynamics before and after mitosis. The prophase-prometaphase and anaphase-telophase transitions were easily identifiable in time-lapse image sequences (Fig. 1C; Videos S1 and S2), allowing us to use these as reference points for timing and duration analyses of INM (Fig. 1D-F). Apically directed INM occurred 27.8 ± 3.5 minutes before the prophase-prometaphase transition, with an average velocity

113 of 0.38 ± 0.05 μm/min (n = 10, Fig. 1D, F). Basally directed INM lasted 26.2 ± 6.4 minutes
114 after telophase, with an average velocity of 0.46 ± 0.09 μm/min (n = 10) (Fig. 1E, F).
115 Although apically directed INM is generally associated with G2 phase of the cell cycle
116 (Baye and Link, 2008; Taverna and Huttner, 2010; Kosodo, 2012), the precise timing of
117 its initiation within G2 remains unclear. To address this, we measured G2 phase duration
118 using BrdU (5-Bromo-2'-deoxyuridine) labeling. Fish embryos were exposed to BrdU at
119 24 hpf, followed by fixation at various time points. Mitotic cells were identified using
120 phospho-histone H3 (pH3) staining (Hendzel et al., 1997), which allowed clear recognition
121 of prophase cells. No BrdU-positive cells were observed entering M phase at 40-, 60-, or
122 80-minutes post-labeling (Fig. 1G). However, BrdU-positive mitotic cells appeared in all
123 embryos at 100, 120, and 140 minutes, indicating that G2 phase lasts between 80 and
124 100 minutes. Since apically directed INM initiates approximately 27.8 minutes before the
125 prophase-prometaphase transition (Fig. 1D), this migration occurs in late G2 phase.
126
127 **INM in mouse epididymis resembles that in zebrafish otic vesicle**
128 To validate our findings in the zebrafish otic vesicle epithelium and determine the timing
129 of basal-to-apical INM, we examined the murine epididymis, a tubular organ composed
130 of simple columnar epithelial cells. Although spatial distribution of mitotic cells along the
131 epididymal tubule at the tissue level has been explored, polarized epithelial cell division
132 has not been studied in the tissue (Fig. 2A)(Robaire and Hinton, 2002; Hirashima and
133 Adachi, 2015). A survey of epididymal cryosections stained for chromatin DNA and pH3
134 revealed that mitotic events peaked around the fifth week postpartum and occurred
135 primarily in the initial segment (Fig. 2A, B). G2-phase nuclei, identified by punctate pH3-
136 positive foci (Hendzel et al., 1997), were observed in both the basal and middle regions
137 (Fig. 2C, panels 1, 3, 4). In contrast, prophase nuclei, marked by chromosome
138 condensation and strong pH3 staining (Hendzel et al., 1997), were found exclusively in
139 the middle-to-apical region (Fig. 2C, panel 2). Prometaphase and metaphase

140 chromosomes clustered apically (Fig. 2C, panels 2-3), while telophase nuclei were
141 observed in the middle region, suggesting a return migration (Fig. 2C, panel 4).
142 Additionally, mitotic cells underwent planar divisions at the apical side (Fig. 2C, panels 2,
143 4), confirming that epithelial cells in the mouse epididymis exhibit characteristic INM and
144 apical division patterns.

145 To further investigate the timing of apically directed INM, mice were injected
146 intraperitoneally with BrdU to label S-phase cells and sacrificed 1-hour post-injection.
147 Among 750 BrdU-positive cells examined, all S-phase nuclei, which were pH3-negative,
148 were located at the basal side (Fig. 2D, 2E). The majority of G2-phase nuclei, identified
149 by dual BrdU and pH3 labeling, were found in the basal region, with a smaller fraction in
150 the middle region (Fig. 2D-E). These findings suggest that INM begins after G2, but not
151 immediately upon, G2 entry.

152 To trace nuclear dynamics during cell cycle progression, we performed a pulse-chase
153 experiment by sacrificing mice at 1, 5, 12, and 24 hours post-BrdU injection. At 1 hour,
154 89.6% of BrdU-positive nuclei were concentrated in the basal region. By 5 and 12 hours,
155 they were distributed across all regions (Fig. 2F-G). At 24 hours, BrdU-positive nuclei
156 peaked again in the basal region (86.4%), with a marked reduction in other regions (Fig.
157 2F-G). Furthermore, BrdU-positive nuclei frequently appeared as pairs at the basal side
158 at 24 hours (Fig. 2F), indicating that daughter cells remained adjacent post-division.
159 These findings suggest that epithelial cells in both the mouse epididymis and the
160 zebrafish otic vesicle exhibit the INM characteristic of proliferative simple columnar
161 epithelia.

162

163 **Cell shape dynamics and basal lamina attachment during INM and mitosis**

164 To gain insights into the mechanisms of INM, we investigated cell shape dynamics during
165 INM and subsequent cell division. In the epididymis, lateral adherens junctions visualized
166 through F-actin or E-cadherin staining (Yap et al., 1997; Baum and Georgiou, 2011)

167 revealed that columnar cell morphology persisted from interphase to prophase (Fig. 3A,
168 B). In prometaphase, cells began to round up while retaining a narrow basal protrusion
169 attached to the basal lamina (Fig. 3A, B, arrowheads), which largely remained throughout
170 cell division (Fig. 3A). Although E-cadherin staining intensity on the lateral cell membrane
171 remained unchanged (Fig. 3B), signals for F-actin, phospho-E-cadherin, and β-catenin
172 were markedly increased in prometaphase and metaphase cells (Fig. 3A-C), suggesting
173 enhanced lateral membrane adhesion between mitotic and neighboring interphase cells
174 (Lickert et al., 2000; Navarro et al., 2005; Bertocchi et al., 2012).

175 To further validate these observations, we examined zebrafish otic vesicle cells
176 labeled with H2B-GFP and RFP-F. As shown in Fig. 1C and Video S2, live imaging
177 revealed that columnar cell morphology was largely maintained during basal-to-apical
178 INM, consistent with observations in the epididymis. From prometaphase, the lateral cell
179 membrane at the basal region gradually collapsed, forming a stalk-like process that
180 remained attached to the basal lamina as the cell body rounded up (Fig. 1C, 32-48',
181 arrowheads). Moreover, cleavage furrow ingression initiated at the basal side of the cell
182 (Fig. 1C, 50', yellow arrow), reaching the apical surface within approximately 2 minutes
183 (Fig. 1C, 52').

184 To further examine cell shape and F-actin dynamics, we expressed GFP-tagged
185 hUtrCH, a fragment of human Utrophin that binds specifically to F-actin without perturbing
186 actin dynamics (Burkel et al., 2007; Norden et al., 2009). Live imaging showed GFP-
187 hUtrCH enrichment at the cell cortex in otic vesicle epithelial cells (Fig. 3D, Video S3),
188 confirming proper F-actin labeling in zebrafish. We observed similar cell shape changes
189 in terms of cell rounding timing (30'-56'), basal lamina attachment (50'-62'), and cleavage
190 furrow ingression (58'-62') (Fig. 3D, arrowheads). Additionally, we detected increased
191 GFP signal intensity during cell rounding and cleavage furrow ingression (Fig. 3D, bottom),
192 indicating the involvement of actomyosin activity in these processes. These findings
193 suggest that columnar epithelial cells round up at prometaphase and undergo mitosis

while maintaining a cellular protrusion anchored to the basal lamina, with cleavage furrow ingression initiating from the basal side of the cell body.

Myosin II activity regulates mitotic cell rounding, spindle orientation, and epithelial Integrity

Our live imaging of F-actin dynamics suggested a role for actomyosin in epithelial cell division. To further investigate the contribution of myosin II-mediated F-actin contraction, we examined its role in zebrafish epithelial cells. In non-muscle cells, myosin II is a well-established actin-associated motor protein that generates contractile forces and has been implicated in INM of neuroepithelia (Norden et al., 2009; Schenk et al., 2009). To assess myosin II function, we treated zebrafish embryos with 100 μM blebbistatin, a small-molecule inhibitor of myosin II activity (Straight et al., 2003). Consistent with previous finding(Norden et al., 2009), blebbistatin treatment did not affect actin polymerization, as GFP-hUtrCH localization remained unchanged compared to controls (Fig. 4A; Videos S4 and S5). The treatment was effective, however, as evidenced by the pronounced cytokinesis defects observed throughout the embryos (Fig. 4A; Videos S4 and S5)(Straight et al., 2003).

Blebbistatin treatment did not alter the frequency of basal-to-apical INM or the average migration velocity (0.38 ± 0.06 μm/min for 16 blebbistatin-treated cells vs. 0.4 ± 0.08 μm/min for 20 vehicle-treated cells) in the otic vesicle (Fig. 4B, C), suggesting that myosin II activity is dispensable for apically directed INM. However, several defects were noted in blebbistatin-treated cells. Firstly, the treated cells failed to round up during mitosis. While 98.3% of vehicle-treated cells (58/59) successfully rounded up after entering prometaphase (Fig. 4D; Video S4), blebbistatin-treated cells largely failed to do so. Instead, 73.1% (38/52) of treated cells maintained a diamond-shaped morphology in prometaphase and metaphase (Fig. 4D; Video S5).

Secondly, although mitosis still occurred at the apical surface, spindle orientation was

221 frequently disrupted. In control cells, 97.6% (41/42) divided at angles between 60°-90°,
222 indicating proper planar spindle orientation (Fig. 4D-F). In contrast, only 39.2% (20/51) of
223 blebbistatin-treated cells maintained this orientation, while another 39.2% divided along
224 the basal-apical axis (0°-30°), demonstrating a severe spindle misorientation defect (Fig.
225 4D-F).

226 Thirdly, in control mitotic cells, both daughter nuclei migrated back to the basal side
227 within ~30 min after anaphase onset (Fig. 4A, D; Video S4). However, in 70.6% of
228 blebbistatin-treated mitotic cells (36/51), one daughter nucleus remained at the apical
229 side for over 50 min (Fig. 4A, D; Video S5). Among these, 33 of the 36 retained nuclei
230 persisted at the apical surface (Fig. 4F, red dots) throughout the imaging period, while
231 only 3 eventually migrated basally. GFP-hUtrCH fluorescence revealed that daughter
232 cells with retained nuclei remained round, indicating a failure to reintegrate into the
233 epithelium (Fig. 4A, D; Video S5). Further analysis revealed a correlation between division
234 angles and nuclear retention. Among blebbistatin-treated mitotic cells with division angles
235 of 0°-60°, 96.8% (30/31) exhibited apical nuclear retention (Fig. 4F, red dots), whereas
236 only 30% (6/20) of those with division angles between 60°-90° retained nuclei apically.
237 Cells positioned closer to the lumen were more likely to be retained (Fig. 4D). These
238 findings suggest that planar division is essential for proper daughter cell integration into
239 the epithelium. Together, our results demonstrate that while cell rounding is not required
240 for M-phase entry, it is crucial for proper spindle orientation and epithelial integrity.

241

242 **Basal-to-apical INM requires microtubules**

243 Both MTs and F-actin have been reported to play essential roles in INM (Baye and Link,
244 2008; Taverna and Huttner, 2010; Kosodo, 2012). To examine the specific contributions
245 of MTs in our INM models, we performed immunostaining against α-tubulin in mouse
246 epididymal epithelium. This revealed MTs oriented along the apicobasal axis of the cell
247 (Fig. 5A). These MTs were largely stable and surrounded migrating nuclei, as indicated

248 by acetylated tubulin (Ace-tu) staining (Fig. 5B, C). Similarly, live imaging of zebrafish otic
249 vesicle epithelium using EMTB-GFP, a live-cell marker for MTs (Bulinski et al., 1999; Faire
250 et al., 1999; Wuhr et al., 2011), showed a comparable MT organization (Fig. 5D; Video
251 S6).

252 To functionally validate these findings, we treated zebrafish embryos with 0.5 μg/ml
253 nocodazole to disrupt MTs. To confirm the drug efficacy, embryos were fixed 120 minutes
254 after treatment, revealing the absence or fragmentation of mitotic spindles in zebrafish
255 otic vesicle mitotic cells, whereas normal spindles were observed in vehicle (DMSO)-
256 treated controls (Fig. 5E, arrows). MTs in interphase cells were also largely disrupted
257 following nocodazole treatment (Fig. 5E).

258 Live imaging from ~20 minutes after nocodazole treatment showed mitotic cells
259 arrested in mitosis (Fig. 5F, arrowhead), confirming drug effectiveness. Time-lapse
260 microscopy further revealed a significant reduction in INM events (Fig. 5F, G; Videos S7
261 and S8). As nocodazole treatment progressively thinned the epithelium, we focused our
262 analysis on the thickest region, located in the anterior-ventral area, from 30 to 236 minutes
263 post-treatment, when epithelial cells remained columnar (Fig. 5F; Video S8). Compared
264 to the vehicle treatment, nocodazole treatment resulted in an average 7.5-fold reduction
265 in INM events (Fig. 5G). These results demonstrate that basal-to-apical INM relies on
266 MTs.

267

268 **Cytoplasmic dynein activity is critical for basal-to-apical INM**

269 Studies in rodent neuroepithelia suggest that cytoplasmic dynein, a microtubule-based
270 minus-end-directed motor protein, plays a major role in mediating basal-to-apical nuclear
271 movement. This function is supported by proteins localized both at the apically anchored
272 centrosome (such as Cep120, TACCs, Hook3, and PCM1), which help maintain
273 microtubule arrays (Gambello et al., 2003; Xie et al., 2007; Ge et al., 2010; Tsai et al.,
274 2010), and at the nuclear membrane (such as Syne1/2 and Sun1/2), which tether the

275 nucleus to dynein (Zhang et al., 2009; Taverna and Huttner, 2010). To assess the role of
276 dynein in INM in the zebrafish otic vesicle epithelium, we overexpressed RFP-tagged
277 human p50, a known inhibitor of dynein activity (Echeverri et al., 1996; Burkhardt et al.,
278 1997; Liang et al., 2007). To minimize potential developmental defects caused by dynein
279 inactivation, we microinjected zebrafish embryos with a plasmid encoding RFP-p50 under
280 the control of the zebrafish hsp70 promoter, followed by heat shock treatment at 20 hpf
281 for 1 hour to induce RFP-p50 expression (Asakawa et al., 2008). Live-cell imaging was
282 performed 1.5 hours after heat shock, when RFP fluorescence became visible. Compared
283 to RFP-expressing controls, RFP-p50 overexpression significantly suppressed apically
284 directed INM (Fig. 5H, 5I; Videos S9, S10). Over a 300-minute observation period, 55 ±
285 10% of RFP-positive otic vesicle cells underwent apical INM, whereas only 21 ± 5% of
286 RFP-p50-expressing cells did (Fig. 5I). These results suggest that cytoplasmic dynein is
287 required for MT-mediated basal-to-apical INM.
288

289 **Nuclear migration is essential for M phase onset**

290 Interestingly, in long columnar cells treated with nocodazole, mitotic entry was observed
291 only at the apical side, after cells had completed INM (Fig. 5F; Video S8). By contrast, in
292 the thinner epithelium of the posterior region, where nuclei are close to the apical
293 membrane, cells frequently entered M phase (Video S8). This difference implies a link
294 between nuclear position and mitotic entry. To investigate this further, immunostaining of
295 mouse epididymal epithelium revealed that centrosomes localized near the apical surface
296 during nuclear migration, and centrioles only moved to opposite sides of the nucleus after
297 it reached the apical side (Fig. 6A). Live imaging using EMTB-GFP to label MTs and MT
298 organizing centers (MTOCs) confirmed this dynamic process in the zebrafish otic vesicle
299 epithelium. The MTOCs remained apically localized until the nuclei reached the apical
300 side (Fig. 6B; Video S6). To explore the molecular mechanisms further, we stained for
301 cyclin B1, a marker of late G2 and M-phase cells. In the mouse epididymis epithelium,

302 Cyclin B1 was localized in the cytoplasm of migrating nuclei and only entered the nuclei
303 once they reached the apex (Fig. 6C, D). this further confirmed that the timing of mitosis
304 coincides with the apical localization of nuclei (Gavet and Pines, 2010; Santos et al.,
305 2012).
306

307 **DISCUSSION**

308 Recent studies using intestinal organoids, neural tube slices, and other cultured models
309 have provided insights into columnar epithelial cell division (Spear and Erickson, 2012;
310 Carroll et al., 2017; Saleh et al., 2023), but these systems often lack the spatial
311 organization and/or biomechanical context of native tissues. *In vivo* models, meanwhile,
312 are typically limited to fixed samples, which precludes dynamic analysis. Although
313 previous studies have characterized the morphogenesis of the zebrafish otic vesicle
314 (Megason, 2009; Hoijman et al., 2015; Mosaliganti et al., 2019), we adapted this system
315 as a live, physiological, and genetically tractable model for real-time visualization of
316 epithelial nuclear dynamics and mitosis, thereby addressing key limitations of earlier
317 approaches. Furthermore, we validated the translatability of our findings using a
318 complementary mammalian model, the mouse epididymal epithelium.
319

320 **Basal-to-apical INM does not start immediately after G2 entry**

321 Our results suggest that basal-to-apical INM begins in the late G2 phase in the zebrafish
322 otic vesicle epithelium (Fig. 1, 7). Similarly, in the mouse epididymis, INM predominantly
323 occurs after G2 initiation (Fig. 2). Interestingly, while nuclear oscillations are frequently
324 observed in neuroepithelia, a rapid, directional basal-to-apical movement occurs just prior
325 to mitosis (Norden et al., 2009; Tsai et al., 2010; Kosodo et al., 2011). This movement
326 appears to initiate in mid-to-late G2 across different epithelial systems. For example,
327 directional INM lasts 5-30 minutes in the developing zebrafish retina (Norden et al., 2009)
328 and approximately 60 minutes in the mouse neural tube[14, 45]. Thus, the late onset of INM

329 during G2 may be a conserved feature across both simple columnar and pseudostratified
330 epithelia.
331
332 **Basal-to-apical INM requires MTs and dynein, but not myosin II**
333 We show that basal-to-apical INM in the zebrafish otic vesicle is dependent on MTs and
334 dynein (Fig. 7). Both p50 overexpression and nocodazole treatment significantly
335 suppressed INM (Fig. 5), whereas myosin II inhibition had little effect (Fig. 4). This is in
336 contrast to neuroepithelia, where MTs, dynein, and actomyosin all contribute to INM
337 (Taverna and Huttner, 2010; Kosodo, 2012). This difference may be attributed to cell
338 shape. In pseudostratified epithelia, nuclei migrate along narrow processes, requiring
339 both MT motor-generated pulling forces and actomyosin-mediated squeezing forces
340 exerted by lateral membrane constriction (Taverna and Huttner, 2010; Kosodo, 2012).
341 However, in columnar epithelia, where cell shape remains unchanged during INM,
342 actomyosin-generated forces become dispensable. Because dynein inhibition or MT
343 disassembly blocked basal-to-apical INM, we could not assess the role of the MT system
344 in basally directed INM in the zebrafish otic vesicle. Similarly, blebbistatin-treated
345 embryos exhibited impaired planar cell division (Fig. 4), preventing us from determining
346 the role of myosin II in apical-to-basal nuclear movement. However, since one or both
347 daughter nuclei were still able to move back to the basal side (Fig. 4), myosin II may be
348 dispensable for apical-to-basal nuclear migration.
349
350 **Mitotic cell rounding and planar division depend on actomyosin**
351 We clarify that mitotic cell rounding in both zebrafish otic vesicle and mouse epididymal
352 epithelium occurs during prometaphase (Fig. 3, 4, and 7). Similar basal adhesion
353 maintenance has been reported in mitotic epithelial cells of the mouse intestine and
354 kidney, suggesting a shared feature in both simple columnar and pseudostratified
355 epithelia (Fleming et al., 2007; Baye and Link, 2008; Taverna and Huttner, 2010; Kosodo,

356 2012; Packard et al., 2013). We show that myosin II is the primary driver of mitotic
357 rounding (Fig. 4). The increased signals of F-actin, phospho-E-cadherin, and β-catenin at
358 lateral membranes (Fig. 3) likely strengthen actomyosin forces, facilitating lateral
359 membrane contraction while maintaining tight adhesion to neighboring interphase cells
360 during mitotic shape remodeling (Fig. 7) (Lickert et al., 2000; Navarro et al., 2005; Qin et
361 al., 2005). Understanding how INM and mitotic rounding are coupled to specific cell cycle
362 stages remains an intriguing avenue for future research. Planar cell division also depends
363 on myosin II activity (Fig. 4), likely because failure of mitotic rounding disrupts spindle
364 orientation. Spindle orientation is biased toward the long axis of the cell (O'Connell and
365 Wang, 2000; Saleh et al., 2023) and requires interactions between the spindle and the
366 cell cortex (Siller and Doe, 2009; Lu and Johnston, 2013). Thus, mitotic rounding may
367 provide the cortical geometry needed for proper spindle alignment and planar division
368 (Campinho et al., 2013; Godard and Heisenberg, 2019; Saleh et al., 2023).
369

370 **Planar cell division facilitates daughter cell integration into the epithelium**

371 In zebrafish otic vesicles treated with blebbistatin, perpendicular divisions (0-30° angles)
372 frequently resulted in apical retention of one daughter cell near the lumen, while the
373 basally positioned daughter nucleus returned to the basal side (Fig. 4). By contrast, planar
374 divisions (60-90° angles) were associated with a significantly reduced incidence of
375 nuclear retention. One possible explanation is that planar division preserves both apical
376 tight junctions(Packard et al., 2013) and basal lamina attachment, maintaining basal-
377 apical polarity of daughter cells (Fig. 7). In contrast, perpendicular division disrupts basal
378 lamina contact, preventing efficient epithelial reintegration. Such defects could
379 compromise otic vesicle structure and function, and the mechanism may also apply to
380 other simple columnar epithelia, where planar division failure disrupts tissue integrity.
381

382 **Mitosis is coupled to INM in the zebrafish otic vesicle epithelium**

383 In neuroepithelia, INM is not required for cell cycle progression. Blocking INM via
384 cytochalasin B treatment or disrupting Lis1/Dynein function allows mitosis to occur
385 throughout the neuroepithelium without halting the cell cycle (Murciano et al., 2002;
386 Gambello et al., 2003; Tsai et al., 2005; Del Bene et al., 2008). However, INM is
387 dependent on cell cycle progression, as cell cycle arrest (e.g., by 5-azacytidine and
388 cyclophosphamide) halts INM (Ueno et al., 2006). In our system, mitosis occurs
389 exclusively at the apical side. Disrupting MTs or dynein activity led to a significant
390 reduction in mitoses, with no mitotic events observed at the basal side in the tall columnar
391 epithelium. This finding aligns with our observation that mitotic spindle formation and
392 nuclear entry of cyclin B occur when nuclei approach the apical side. Future research
393 should investigate whether apically localized signals, such as centrosome-associated
394 components, contribute to M-phase onset.
395

396 **Limitations of the study**

397 Here, we demonstrated the use of the zebrafish embryonic otic vesicle epithelium as a
398 model for investigating epithelial cell division in a physiological context with a focus on
399 nuclear migration, cell shape dynamics, and spindle orientation. However, several
400 technical limitations should be considered. First, we utilized microinjection of *in vitro*
401 synthesized mRNA to label histones, F-actin, MTs to demonstrate the feasibility of this
402 approach. To enhance consistency and minimize potential toxicity from ectopic transgene
403 expression, available stable transgenic lines could be used. For example, the
404 *h2afv:h2afv-mCherry* (Knopf et al., 2011) or *hsp70:H2B-RFP* (Dzafic et al., 2015) line can
405 serve as a histone marker, while *actb2:mCherry-UTRN* (Compagnon et al., 2014) or
406 *actb1:lifeact-GFP* (Behrndt et al., 2012) can be used for F-actin labeling. Additionally,
407 Fluorescent Ubiquitin-Mediated Cell Cycle Indicator (FUCCI) reporters (Sakaue-Sawano
408 et al., 2008; Bouldin et al., 2014) provide a powerful tool for tracking cell cycle progression.
409 Various inducible transgenic tools are also widely available for conditional gene

manipulation in zebrafish embryos. Second, our live imaging experiments were performed using an inverted confocal microscope, requiring careful orientation of the embryos so that the otic vesicle is positioned close to the glass bottom of the mounting dish for optimal imaging quality. The use of an upright microscope equipped with high-NA water immersion objectives would simplify sample mounting and improve resolution. Additionally, spinning-disk microscopy could further enhance spatiotemporal resolution. Third, the morphology of the zebrafish embryonic otic vesicle evolves rapidly, with a limited window of approximately six hours (22–28 hpf) during which the ventral side maintains a columnar epithelial structure. This constraint makes it less suitable for studies requiring extended observation periods. Nonetheless, this live imaging system provides an unprecedented opportunity to explore epithelial cell division in a natural physiological context, offering valuable insights into cellular and molecular dynamics.

423 **Materials and Methods**

424 **Animals**

425 All animal procedures were conducted in accordance with protocols approved by the
426 Institutional Animal Care and Use Committee (IACUC). Zebrafish (Ekkwill (EK) and AB
427 strains) were raised under standard conditions and staged in hours post-fertilization (hpf)
428 as previously described (Kimmel et al., 1995; Westerfield, 2000). Male C57BL/6J mice 3-
429 12 weeks old were obtained from Jackson Laboratories and maintained under a 12-hour
430 light/dark cycle at a constant temperature of 22°C.

431

432 **Plasmid constructs**

433 To express RFP-F, the open reading frame (ORF) of monomeric RFP (mRFP) from
434 pmRFP-C1 (Li et al., 2007) was fused to the c-Ha-Ras farnesylation signal (Hancock et
435 al., 1991; Aronheim et al., 1994) via PCR. For GFP-UtrCH expression, the first 783 base
436 pairs of the human utrophin coding sequence (Burkel et al., 2007; Norden et al., 2009)
437 were PCR-amplified and inserted in-frame into the BspEI-XhoI sites of pEGFP-C1. For *in*
438 *vitro* mRNA transcription, the ORFs for H2B-GFP (Liang et al., 2007), H2B-RFP (Li et al.,
439 2007), RFP-F, GFP-hUtrCH, and EMTB-GFP (Wuhr et al., 2011) were subcloned into
440 pCS2^{+}. For heat shock-inducible expression of RFP or RFP-p50, the ORFs were PCR-
441 amplified and inserted into the BamHI-NheI sites of pT2KhspGFF (Asakawa et al., 2008).
442 pT2KhspGFF and pCS-TP, which encodes a transposase required for stable integration
443 of pT2KhspGFF into genomic DNA (Kawakami et al., 2004), were generously provided
444 by Dr. K. Kawakami (Graduate University for Advanced Studies, Japan). All plasmids
445 containing PCR-amplified fragments were confirmed by sequencing.

446

447 **Zebrafish microinjection**

448 *In vitro* mRNA synthesis was performed using the mMessage mMachine SP6 kit (Thermo
449 Fisher, AM1340). For yolk injections, 5 nL of transcribed mRNA was injected, while for

450 cytoplasmic injections, 1 nL of a plasmid-mRNA mixture was delivered into fertilized eggs.
451 Phenol red (0.02%) was included as a tracer. For yolk injections, mRNAs encoding H2B-
452 GFP, H2B-RFP, GFP-hUtrCH, or EMTB-GFP were used at a concentration of 50 ng/μL,
453 while RFP-F mRNA was injected at 75 ng/μL. For cytoplasmic injections, a mixture
454 containing H2B-GFP mRNA (20 ng/μL), TP mRNA (30 ng/μL), and a heat shock-inducible
455 plasmid (30 ng/μL) was used. To induce gene expression, heat shock was applied for one
456 hour at 39°C in a water bath starting at approximately 20 hpf.
457

458 **BrdU incorporation**

459 For mouse experiments, C57BL/6 mice received intraperitoneal injections of BrdU at a
460 dose of 100 μg per gram of body weight, followed by sacrifice at different time points. The
461 epididymides were dissected and fixed overnight in 4% paraformaldehyde (PFA) in PBS
462 at 4°C. BrdU labeling in zebrafish was performed as previously described(Shepard et al.,
463 2004). Briefly, at 24 hpf, embryos were dechorionated and incubated in 10 mM BrdU
464 (Millipore Sigma, B5002) in embryo medium for 20 minutes on ice. They were then
465 transferred to warm medium and incubated for an additional 40 to 140 minutes at 28.5°C.
466 After incubation, embryos were fixed overnight in PFA and subsequently dehydrated in
467 graded methanol in PBT (PBS containing 0.1% Tween-20).
468

469 **Immunofluorescence microscopy**

470 Mouse epididymal cryosections were prepared at a thickness of 10 μm and processed for
471 staining as previously described (Wang et al., 2008). Briefly, tissue samples were blocked
472 in PBS containing 10% goat serum and 0.5% Triton X-100 for one hour, followed by
473 overnight incubation with primary antibodies at 4°C. After extensive washing, secondary
474 antibodies were applied for 1.5 hours at room temperature. For BrdU staining,
475 cryosections were denatured in 2 M HCl for 15 minutes at 37°C, neutralized in 0.1 M
476 $Na_2B_4O_7$ for 10 minutes at room temperature, and rinsed three times in PBS before

477 incubation with an anti-BrdU antibody at a 1:1000 dilution. Whole-mount immunostaining
478 of zebrafish embryos followed established protocols (Wloga et al., 2009). BrdU staining
479 was performed by digesting rehydrated embryos with proteinase K (10 μg/mL, Fisher
480 Scientific, BP1700-100) for 10 minutes at room temperature, followed by fixation in PFA
481 for 20 minutes. Embryos were incubated in 2 M HCl for one hour, washed three times in
482 PBT, and then subjected to immunostaining (Shepard et al., 2004). The primary
483 antibodies used in this study included mouse monoclonal antibodies against α-tubulin
484 (Millipore Sigma, T6199) and BrdU (Millipore Sigma, SAB4700630), rabbit antibodies
485 against phospho-histone H3 (Ser10) (Cell Signaling Technology, 9701), phospho-E-
486 cadherin (Ser838/840; Novus Biologicals, NBP3-12922), and β-catenin (Millipore Sigma,
487 C2206), as well as a rat monoclonal antibody against E-cadherin (Abcam, ab11512).
488 Secondary antibodies (ThermoFisher) used in this study were Alexa Fluor 488 goat anti-
489 rabbit (A11034), goat anti-rat (A11006) and goat anti-mouse (A11029), and Alexa Fluor
490 546 goat anti-rabbit (A11035) and goat anti-mouse (A11030). Phalloidin-TRITC (P1951)
491 and DAPI (D9542) were from Millipore Sigma. Fixed samples were imaged using Leica
492 TCS SP5 or Zeiss LSM 800 confocal microscope.
493
494 **Live cell imaging**
495 Embryos were first screened at 22 hpf under a Zeiss Axio Zoom V16 fluorescent
496 dissecting microscope to identify those with GFP or RFP expression in the otic vesicles.
497 Selected embryos were dechorionated, anesthetized with tricaine (Sigma-Aldrich,
498 E10521), mounted in 1% low-melting point agarose (Fisher Scientific, BP1360-100) within
499 a glass-bottom Petri dish (MatTek Life Sciences, P35G-1.5-14-C), and covered with E2
500 embryo medium containing tricaine and 0.003% phenylthiourea (Millipore Sigma, P7629).
501 For experiments involving drug treatments, blebbistatin (100 μM, Millipore Sigma, B0560),
502 nocodazole (0.5 μg/ml, Millipore Sigma, M1404), or DMSO (Millipore Sigma, D8418) as
503 the solvent control was added to both the medium and agarose. Embryos were positioned

504 so that one otic vesicle was in close proximity to the glass bottom. Time-lapse imaging
505 was conducted at 2-minute intervals over a period of 216 to 430 minutes using a 20× NA
506 0.7 objective on a Leica TCS SP5 or Zeiss LSM 800 inverted confocal microscope
507 equipped with a heating hood.
508

509 **Statistical analysis of nuclear migration**

510 Nuclear displacement was quantified as the distance between the bottom edge of the
511 nucleus and the basal membrane(Norden et al., 2009). Measurements were taken at 2-
512 minute intervals using ImageJ software. Instantaneous velocity (v_i) was generate using
513 formula $v_i = (p_{i+1} - p_i) / (t_{i+1} - t_i)$ (Norden et al., 2009). where p represents position, t represents
514 time, and i denotes the time point. Positive values indicated apical migration, while
515 negative values represented basal migration. Quantification values are reported as mean
516 ± S.D. Student's *t*-tests (two-tailed) were applied when normality and equal variance tests
517 were passed.
518

Acknowledgements

We thank A. Afolalu, C. Shapiro, S. Hosten, and C. Quaies for fish care; Dr. Koichi Kawakami (National Institute of Genetics and Department of Genetics, Graduate University for Advanced Studies, Japan) for providing the pT2KhspGFF and pCS-TP constructs; Zhili Wu and Yiping Li for technical support; and Xueliang Zhu for guidance and comments on the manuscript. This work was supported by The Louis and Rachel Rudin Foundation fellowship to Y.X., a New York State Stem Cell Science program (NYSTEM) predoctoral training grant position to B.P., and National Institutes of Health (NIH) grants R01HL155607 and R01HL166518 to J.C.

Author contributions

Conceptualization: J.C.

Methodology: Y.X. and J.C.

Investigation: Y.X., B.P., A.G.C.Y., and M.Q.

Resources: J.C.

Writing and editing: Y.X., B.P., and J.C.

Funding Acquisition: J.C.

Declaration of interest

The authors declare no competing interests.

References

Ahringer, J. (2003) Control of cell polarity and mitotic spindle positioning in animal cells, *Curr Opin Cell Biol* 15(1): 73-81.

Aronheim, A., Engelberg, D., Li, N., al-Alawi, N., Schlessinger, J. and Karin, M. (1994) Membrane targeting of the nucleotide exchange factor Sos is sufficient for activating the Ras signaling pathway, *Cell* 78(6): 949-61.

Asakawa, K., Suster, M. L., Mizusawa, K., Nagayoshi, S., Kotani, T., Urasaki, A., Kishimoto, Y., Hibi, M. and Kawakami, K. (2008) Genetic dissection of neural circuits by Tol2 transposon-mediated Gal4 gene and enhancer trapping in zebrafish, *Proc Natl Acad Sci U S A* 105(4): 1255-60.

Bagley, D. C., Russell, T., Ortiz-Zapater, E., Stinson, S., Fox, K., Redd, P. F., Joseph, M., Deering-Rice, C., Reilly, C., Parsons, M. et al. (2024) Bronchoconstriction damages airway epithelia by crowding-induced excess cell extrusion, *Science* 384(6691): 66-73.

Baum, B. and Georgiou, M. (2011) Dynamics of adherens junctions in epithelial establishment, maintenance, and remodeling, *J Cell Biol* 192(6): 907-17.

Baye, L. M. and Link, B. A. (2008) Nuclear migration during retinal development, *Brain Res* 1192: 29-36.

Behrndt, M., Salbreux, G., Campinho, P., Hauschild, R., Oswald, F., Roensch, J., Grill, S. W. and Heisenberg, C. P. (2012) Forces driving epithelial spreading in zebrafish gastrulation, *Science* 338(6104): 257-60.

Bergstralh, D. T., Lovegrove, H. E., Kujawiak, I., Dawney, N. S., Zhu, J., Cooper, S., Zhang, R. and St Johnston, D. (2016) Pins is not required for spindle orientation in the Drosophila wing disc, *Development* 143(14): 2573-81.

Bertocchi, C., Vaman Rao, M. and Zaidel-Bar, R. (2012) Regulation of adherens junction dynamics by phosphorylation switches, *J Signal Transduct* 2012: 125295.

Bouldin, C. M., Snelson, C. D., Farr, G. H., 3rd and Kimelman, D. (2014) Restricted expression of cdc25a in the tailbud is essential for formation of the zebrafish posterior body, *Genes Dev* 28(4): 384-95.

Bulinski, J. C., Gruber, D., Faire, K., Prasad, P. and Chang, W. (1999) GFP chimeras of E-MAP-115 (ensconsin) domains mimic behavior of the endogenous protein in vitro and in vivo, *Cell Struct Funct* 24(5): 313-20.

Burkel, B. M., von Dassow, G. and Bement, W. M. (2007) Versatile fluorescent probes for actin filaments based on the actin-binding domain of utrophin, *Cell Motil Cytoskeleton* 64(11): 822-32.

Burkhardt, J. K., Echeverri, C. J., Nilsson, T. and Vallee, R. B. (1997) Overexpression of the dynamitin (p50) subunit of the dynactin complex disrupts dynein-dependent maintenance of membrane organelle distribution, *J Cell Biol* 139(2): 469-84.

Campinho, P., Behrndt, M., Ranft, J., Risler, T., Minc, N. and Heisenberg, C. P. (2013) Tension-oriented cell divisions limit anisotropic tissue tension in epithelial spreading during zebrafish epiboly, *Nat Cell Biol* 15(12): 1405-14.

Carroll, T. D., Langlands, A. J., Osborne, J. M., Newton, I. P., Appleton, P. L. and Nathke, I. (2017) Interkinetic nuclear migration and basal tethering facilitates post-mitotic daughter separation in intestinal organoids, *J Cell Sci* 130(22): 3862-3877.

Compagnon, J., Barone, V., Rajshekar, S., Kottmeier, R., Pranjic-Ferscha, K., Behrndt, M. and

581 Heisenberg, C. P. (2014) The notochord breaks bilateral symmetry by controlling cell shapes in the
582 zebrafish laterality organ, *Dev Cell* 31(6): 774-83.
583 Del Bene, F., Wehman, A. M., Link, B. A. and Baier, H. (2008) Regulation of neurogenesis by interkinetic
584 nuclear migration through an apical-basal notch gradient, *Cell* 134(6): 1055-65.
585 Dzafic, E., Strzyz, P. J., Wilsch-Brauninger, M. and Norden, C. (2015) Centriole Amplification in
586 Zebrafish Affects Proliferation and Survival but Not Differentiation of Neural Progenitor Cells, *Cell Rep*
587 13(1): 168-182.
588 Echeverri, C. J., Paschal, B. M., Vaughan, K. T. and Vallee, R. B. (1996) Molecular characterization of the
589 50-kD subunit of dynactin reveals function for the complex in chromosome alignment and spindle
590 organization during mitosis, *J Cell Biol* 132(4): 617-33.
591 Faire, K., Waterman-Storer, C. M., Gruber, D., Masson, D., Salmon, E. D. and Bulinski, J. C. (1999) E-
592 MAP-115 (ensconsin) associates dynamically with microtubules in vivo and is not a physiological
593 modulator of microtubule dynamics, *J Cell Sci* 112 (Pt 23): 4243-55.
594 Fleming, E. S., Zajac, M., Moschenross, D. M., Montrose, D. C., Rosenberg, D. W., Cowan, A. E. and
595 Tirnauer, J. S. (2007) Planar spindle orientation and asymmetric cytokinesis in the mouse small intestine,
596 *J Histochem Cytochem* 55(11): 1173-80.
597 Fujita, S. (1960) Mitotic pattern and histogenesis of the central nervous system, *Nature* 185: 702-3.
598 Fujita, S. (1962) Kinetics of cellular proliferation, *Exp Cell Res* 28: 52-60.
599 Gambello, M. J., Darling, D. L., Yingling, J., Tanaka, T., Gleeson, J. G. and Wynshaw-Boris, A. (2003)
600 Multiple dose-dependent effects of Lis1 on cerebral cortical development, *J Neurosci* 23(5): 1719-29.
601 Gavet, O. and Pines, J. (2010) Activation of cyclin B1-Cdk1 synchronizes events in the nucleus and the
602 cytoplasm at mitosis, *J Cell Biol* 189(2): 247-59.
603 Ge, X., Frank, C. L., Calderon de Anda, F. and Tsai, L. H. (2010) Hook3 interacts with PCM1 to regulate
604 pericentriolar material assembly and the timing of neurogenesis, *Neuron* 65(2): 191-203.
605 Godard, B. G. and Heisenberg, C. P. (2019) Cell division and tissue mechanics, *Curr Opin Cell Biol* 60:
606 114-120.
607 Hancock, J. F., Cadwallader, K., Paterson, H. and Marshall, C. J. (1991) A CAAX or a CAAL motif and a
608 second signal are sufficient for plasma membrane targeting of ras proteins, *EMBO J* 10(13): 4033-9.
609 Hendzel, M. J., Wei, Y., Mancini, M. A., Van Hooser, A., Ranalli, T., Brinkley, B. R., Bazett-Jones, D. P.
610 and Allis, C. D. (1997) Mitosis-specific phosphorylation of histone H3 initiates primarily within
611 pericentromeric heterochromatin during G2 and spreads in an ordered fashion coincident with mitotic
612 chromosome condensation, *Chromosoma* 106(6): 348-60.
613 Hirashima, T. and Adachi, T. (2015) Procedures for the quantification of whole-tissue
614 immunofluorescence images obtained at single-cell resolution during murine tubular organ development,
615 *PloS one* 10(8): e0135343.
616 Hoijman, E., Rubbini, D., Colombelli, J. and Alsina, B. (2015) Mitotic cell rounding and epithelial
617 thinning regulate lumen growth and shape, *Nat Commun* 6: 7355.
618 Ipponjima, S., Hibi, T. and Nemoto, T. (2016) Three-Dimensional Analysis of Cell Division Orientation in
619 Epidermal Basal Layer Using Intravital Two-Photon Microscopy, *PloS one* 11(9): e0163199.
620 Kawakami, K., Takeda, H., Kawakami, N., Kobayashi, M., Matsuda, N. and Mishina, M. (2004) A
621 transposon-mediated gene trap approach identifies developmentally regulated genes in zebrafish, *Dev Cell*

622 7(1): 133-44.
623 Kimmel, C. B., Ballard, W. W., Kimmel, S. R., Ullmann, B. and Schilling, T. F. (1995) Stages of
624 embryonic development of the zebrafish, *Dev Dyn* 203(3): 253-310.
625 Knopf, F., Hammond, C., Chekuru, A., Kurth, T., Hans, S., Weber, C. W., Mahatma, G., Fisher, S., Brand,
626 M., Schulte-Merker, S. et al. (2011) Bone regenerates via dedifferentiation of osteoblasts in the zebrafish
627 fin, *Dev Cell* 20(5): 713-24.
628 Kosodo, Y. (2012) Interkinetic nuclear migration: beyond a hallmark of neurogenesis, *Cell Mol Life Sci*
629 69(16): 2727-38.
630 Kosodo, Y., Suetsugu, T., Suda, M., Mimori-Kiyosue, Y., Toida, K., Baba, S. A., Kimura, A. and
631 Matsuzaki, F. (2011) Regulation of interkinetic nuclear migration by cell cycle-coupled active and passive
632 mechanisms in the developing brain, *EMBO J* 30(9): 1690-704.
633 Lee, C., Goolsby, C. L. and Sensibar, J. A. (1994) Cell cycle kinetics in rat prostatic epithelia: nuclear
634 migration during G2 phase, *J Urol* 152(6 Pt 2): 2294-9.
635 Li, Y., Yu, W., Liang, Y. and Zhu, X. (2007) Kinetochore dynein generates a poleward pulling force to
636 facilitate congression and full chromosome alignment, *Cell Res* 17(8): 701-12.
637 Liang, Y., Yu, W., Li, Y., Yu, L., Zhang, Q., Wang, F., Yang, Z., Du, J., Huang, Q., Yao, X. et al. (2007)
638 Nudel modulates kinetochore association and function of cytoplasmic dynein in M phase, *Mol Biol Cell*
639 18(7): 2656-66.
640 Lickert, H., Bauer, A., Kemler, R. and Stappert, J. (2000) Casein kinase II phosphorylation of E-cadherin
641 increases E-cadherin/beta-catenin interaction and strengthens cell-cell adhesion, *J Biol Chem* 275(7):
642 5090-5.
643 Lu, M. S. and Johnston, C. A. (2013) Molecular pathways regulating mitotic spindle orientation in animal
644 cells, *Development* 140(9): 1843-56.
645 Megason, S. G. (2009) In toto imaging of embryogenesis with confocal time-lapse microscopy, *Methods*
646 *Mol Biol* 546: 317-32.
647 Moore, J. L., Bhaskar, D., Gao, F., Matte-Martone, C., Du, S., Lathrop, E., Ganesan, S., Shao, L., Norris,
648 R., Campama Sanz, N. et al. (2023) Cell cycle controls long-range calcium signaling in the regenerating
649 epidermis, *J Cell Biol* 222(7).
650 Morin, X. and Bellaiche, Y. (2011) Mitotic spindle orientation in asymmetric and symmetric cell divisions
651 during animal development, *Dev Cell* 21(1): 102-19.
652 Mosaliganti, K. R., Swinburne, I. A., Chan, C. U., Obholzer, N. D., Green, A. A., Tanksale, S.,
653 Mahadevan, L. and Megason, S. G. (2019) Size control of the inner ear via hydraulic feedback, *Elife* 8.
654 Murciano, A., Zamora, J., Lopez-Sanchez, J. and Frade, J. M. (2002) Interkinetic nuclear movement may
655 provide spatial clues to the regulation of neurogenesis, *Mol Cell Neurosci* 21(2): 285-300.
656 Nakajima, Y. I., Lee, Z. T., McKinney, S. A., Swanson, S. K., Florens, L. and Gibson, M. C. (2019)
657 Junctional tumor suppressors interact with 14-3-3 proteins to control planar spindle alignment, *J Cell Biol*
658 218(6): 1824-1838.
659 Navarro, C., Nola, S., Audebert, S., Santoni, M. J., Arsanto, J. P., Ginestier, C., Marchetto, S., Jacquemier,
660 J., Isnardon, D., Le Bivic, A. et al. (2005) Junctional recruitment of mammalian Scribble relies on E-
661 cadherin engagement, *Oncogene* 24(27): 4330-9.
662 Norden, C., Young, S., Link, B. A. and Harris, W. A. (2009) Actomyosin is the main driver of interkinetic

663 nuclear migration in the retina, *Cell* 138(6): 1195-208.
664 O'Connell, C. B. and Wang, Y. L. (2000) Mammalian spindle orientation and position respond to changes
665 in cell shape in a dynein-dependent fashion, *Mol Biol Cell* 11(5): 1765-74.
666 Packard, A., Georgas, K., Michos, O., Riccio, P., Cebrian, C., Combes, A. N., Ju, A., Ferrer-Vaquer, A.,
667 Hadjantonakis, A. K., Zong, H. et al. (2013) Luminal Mitosis Drives Epithelial Cell Dispersal within the
668 Branching Ureteric Bud, *Dev Cell* 27(3): 319-30.
669 Qin, Y., Capaldo, C., Gumbiner, B. M. and Macara, I. G. (2005) The mammalian Scribble polarity protein
670 regulates epithelial cell adhesion and migration through E-cadherin, *J Cell Biol* 171(6): 1061-71.
671 Robaire, B. and Hinton, B. T. (2002) *The Epididymis: From Molecules to Clinical Practice*, New York,
672 NY: Kluwer Academic and Plenum Publishers.
673 Rodriguez-Boulan, E. and Macara, I. G. (2014) Organization and execution of the epithelial polarity
674 programme, *Nat Rev Mol Cell Biol* 15(4): 225-42.
675 Sakaue-Sawano, A., Kurokawa, H., Morimura, T., Hanyu, A., Hama, H., Osawa, H., Kashiwagi, S.,
676 Fukami, K., Miyata, T., Miyoshi, H. et al. (2008) Visualizing spatiotemporal dynamics of multicellular
677 cell-cycle progression, *Cell* 132(3): 487-98.
678 Saleh, J., Fardin, M. A., Barai, A., Soleilhac, M., Frenoy, O., Gaston, C., Cui, H., Dang, T., Gaudin, N.,
679 Vincent, A. et al. (2023) Length limitation of astral microtubules orients cell divisions in murine intestinal
680 crypts, *Dev Cell* 58(17): 1519-1533 e6.
681 Santos, S. D., Wollman, R., Meyer, T. and Ferrell, J. E., Jr. (2012) Spatial positive feedback at the onset of
682 mitosis, *Cell* 149(7): 1500-13.
683 Sauer, F. C. (1935) Mitosis in the neural tube, *The Journal of Comparative Neurology* 62: 377-397.
684 Schenk, J., Wilsch-Brauninger, M., Calegari, F. and Huttner, W. B. (2009) Myosin II is required for
685 interkinetic nuclear migration of neural progenitors, *Proc Natl Acad Sci U S A* 106(38): 16487-92.
686 Shepard, J. L., Stern, H. M., Pfaff, K. L. and Amatruda, J. F. (2004) Analysis of the cell cycle in zebrafish
687 embryos, *Methods Cell Biol* 76: 109-25.
688 Siller, K. H. and Doe, C. Q. (2009) Spindle orientation during asymmetric cell division, *Nat Cell Biol*
689 11(4): 365-74.
690 Spear, P. C. and Erickson, C. A. (2012) Apical movement during interkinetic nuclear migration is a two-
691 step process, *Dev Biol* 370(1): 33-41.
692 Straight, A. F., Cheung, A., Limouze, J., Chen, I., Westwood, N. J., Sellers, J. R. and Mitchison, T. J.
693 (2003) Dissecting temporal and spatial control of cytokinesis with a myosin II Inhibitor, *Science*
694 299(5613): 1743-7.
695 Taverna, E. and Huttner, W. B. (2010) Neural Progenitor Nuclei IN Motion, *Neuron* 67(6): 906-914.
696 Tsai, J. W., Chen, Y., Kriegstein, A. R. and Vallee, R. B. (2005) LIS1 RNA interference blocks neural stem
697 cell division, morphogenesis, and motility at multiple stages, *J Cell Biol* 170(6): 935-45.
698 Tsai, J. W., Lian, W. N., Kemal, S., Kriegstein, A. R. and Vallee, R. B. (2010) Kinesin 3 and cytoplasmic
699 dynein mediate interkinetic nuclear migration in neural stem cells, *Nat Neurosci* 13(12): 1463-71.
700 Tsue, T. T., Watling, D. L., Weisleder, P., Coltrera, M. D. and Rubel, E. W. (1994) Identification of hair
701 cell progenitors and intermitotic migration of their nuclei in the normal and regenerating avian inner ear, *J*
702 *Neurosci* 14(1): 140-52.
703 Ueno, M., Katayama, K., Yamauchi, H., Nakayama, H. and Doi, K. (2006) Cell cycle progression is

704 required for nuclear migration of neural progenitor cells, *Brain Res* 1088(1): 57-67.
705 Wang, F., Zhang, Q., Cao, J., Huang, Q. and Zhu, X. (2008) The microtubule plus end-binding protein
706 EB1 is involved in Sertoli cell plasticity in testicular seminiferous tubules, *Exp Cell Res* 314(1): 213-26.
707 Westerfield, Monte (2000) *The zebrafish book. A guide for the laboratory use of zebrafish (Danio rerio).* ,
708 Eugene: University of Oregon Press.
709 Wloga, D., Webster, D. M., Rogowski, K., Bre, M. H., Levilliers, N., Jerka-Dziadosz, M., Janke, C.,
710 Dougan, S. T. and Gaertig, J. (2009) TTLL3 Is a tubulin glycine ligase that regulates the assembly of cilia,
711 *Dev Cell* 16(6): 867-76.
712 Wuhr, M., Obholzer, N. D., Megason, S. G., Detrich, H. W., 3rd and Mitchison, T. J. (2011) Live imaging
713 of the cytoskeleton in early cleavage-stage zebrafish embryos, *Methods Cell Biol* 101: 1-18.
714 Xie, Z., Moy, L. Y., Sanada, K., Zhou, Y., Buchman, J. J. and Tsai, L. H. (2007) Cep120 and TACCs
715 control interkinetic nuclear migration and the neural progenitor pool, *Neuron* 56(1): 79-93.
716 Xin, T., Gallini, S., Wei, H., Gonzalez, D. G., Matte-Martone, C., Machida, H., Fujiwara, H., Pasolli, H.
717 A., Suozzi, K. C., Gonzalez, L. E. et al. (2024) Oncogenic Kras induces spatiotemporally specific tissue
718 deformation through converting pulsatile into sustained ERK activation, *Nat Cell Biol* 26(6): 859-867.
719 Yap, A. S., Brieher, W. M. and Gumbiner, B. M. (1997) Molecular and functional analysis of cadherin-
720 based adherens junctions, *Annu Rev Cell Dev Biol* 13: 119-46.
721 Zhang, X., Lei, K., Yuan, X., Wu, X., Zhuang, Y., Xu, T., Xu, R. and Han, M. (2009) SUN1/2 and
722 Syne/Nesprin-1/2 complexes connect centrosome to the nucleus during neurogenesis and neuronal
723 migration in mice, *Neuron* 64(2): 173-87.

724

725 **Figure legends**

726 **Figure 1. INM in zebrafish otic vesicle epithelium begins in late G2.**

727 **(A)** Schematic of the zebrafish otic vesicle at approximately 22 hpf.

728 **(B)** Morphology of the otic vesicle epithelium at 22 hpf and 28 hpf. Embryos were
729 microinjected with mRNA to express H2B-GFP (chromatin, green) and RFP-F (cell
730 membrane, red). The boxed regions indicate areas used for INM analyses. Scale bar, 20
731 μm.

732 **(C)** Selected frames from Video S2. H2B-GFP (green) and RFP-F (red) label chromatin
733 and the plasma membrane, respectively. Single-channel images of RFP-F are shown in
734 the middle. White arrows indicate the nucleus or chromosomes of the tracked cell, white
735 arrowheads highlight its basal protrusion and plasma membrane, and yellow arrows
736 denote the cleavage furrow. The cell boundary and nucleolus of the tracked cell are
737 outlined below. Scale bar, 20 μm.

738 **(D, E)** Nuclear trajectories before prometaphase (D) and after telophase (E). For daughter
739 nuclei, only one that could be clearly tracked was analyzed.

740 **(F)** Velocity of pooled nuclear movements.

741 **(G)** Estimation of G2 length. Embryos at 24 hpf were labeled with BrdU, fixed at the
742 indicated time points, and stained to visualize BrdU (red), pH3 (green), and DAPI (blue).
743 Representative S-phase cells (arrowheads) and mitotic cells (pH3-positive, arrows) are
744 shown. Yellow dashed lines indicate the basal membrane. Scale bar, 10 μm.

745

746 **Figure 2. INM in the mouse epididymis resembles that in the zebrafish otic vesicle.**

747 **(A)** Schematic of the anatomical structure of the mouse epididymis.

748 **(B)** Quantification of mitotic events per epididymal tubular cross-section. Mitotic cells were
749 identified based on chromosome morphology and/or strong pH3 staining (see C). The
750 number of analyzed tubular cross-sections is indicated above each bar.

751 **(C)** Section images showing nuclear positioning at different cell cycle stages. Insets

752 display pH3 (green) or DAPI (red) staining of the indicated nuclei. Yellow lines mark the
753 apical surface. Scale bar, 20 μm.
754 **(D, E)** Section images and quantification (E) showing S-phase and G2-phase nuclei 1
755 hour after BrdU labeling. Scale bar, 20 μm.
756 **(F, G)** Section images and quantification showing the distribution of BrdU-positive nuclei
757 or chromosome clusters at the indicated time points. Arrows in (F) indicate representative
758 nuclei or chromosome clusters. Scale bar, 20 μm.
759
760 **Figure 3. Cell shape dynamics and basal lamina attachment during INM and mitosis.**
761 **(A-C)** Section images of mouse epididymis epithelium showing cell-cell interfaces labeled
762 with the indicated markers (green). Insets show pH3 staining (magenta) in G2 or
763 prophase cells. Arrows indicate G2 or M-phase cells, and arrowheads point to the narrow
764 basal protrusions of mitotic cells. DAPI staining is shown in red. Fluorescent intensity of
765 F-action signals in (A) is shown at the bottom. Scale bars, 10 μm.
766 **(D)** Selected frames from Video S3 showing GFP-hUtCH (green) and H2B-RFP (red).
767 Single-channel GFP-hUtCH images are shown in grayscale at the bottom. Arrows indicate
768 the nucleus or chromosomes of the tracked cell, while arrowheads highlight its basal
769 process and plasma membrane. Fluorescent intensity of GFP signals is shown at the
770 bottom. Scale bar, 10 μm.
771
772 **Figure 4. Myosin II activity regulates mitotic cell rounding, spindle orientation, and**
773 **epithelial Integrity.**
774 **(A)** Selected frames from Videos S4 and S5 showing INM events. H2B-RFP (red) and
775 GFP-hUtrCH (green) are shown. Time is indicated relative to the addition of DMSO or
776 blebbistatin. Each number represents a nuclear migration event and marks a mitotic cell.
777 Scale bar, 20 μm.
778 **(B)** Quantification of INM events during a 230-min window while epithelial cells remained

779 columnar, starting 20 or 25 min after drug addition. Student's *t*-test.

780 **(C)** Quantification of migration speed of pooled apically directed INM. Student's *t*-test.

781 **(D)** Representative images from Videos S4 and S5 showing mitotic rounding, planar
782 division, and daughter cell insertion after treatment. The locations of mitotic cells in the
783 otic vesicle are indicated in (A) by the corresponding numbers. Arrows indicate parental
784 or daughter nuclei. Scale bar, 10 μm.

785 **(E)** Representative frames showing spindle orientation with GFP-EMTB (green) and H2B-
786 RFP (red). Scale bar, 10 μm.

787 **(F)** Statistical analysis of cell division angles. Each mitotic cell is represented as a dot in
788 the radial histogram. Cells with apically retained daughter nuclei are highlighted in red.

789

790 **Figure 5. INM in zebrafish otic vesicle requires MTs and dynein.**

791 **(A, B)** Section images of epididymal epithelium stained for α-tubulin (A, green), acetylated
792 tubulin (Ace-tu, B, green), pH3 (red), and DAPI (blue). Arrows indicate $pH3^+$ cells, and
793 arrowheads highlight microtubule bundles. Scale bars, 20 μm.

794 **(C)** Z-stack images of the same cell as in (B), showing Ace-tu (green) and DAPI (red)
795 staining.

796 **(D)** Video frame showing EMTB-GFP (green) and H2B-RFP (red). Scale bar, 20 μm.

797 **(E)** Nocodazole-induced microtubule disassembly. Zebrafish otic vesicle was stained for
798 α-tubulin (green) and pH3 (red). DAPI (blue) staining is also shown. Single-channel α-
799 tubulin images are displayed in grayscale at the bottom. Scale bar, 20 μm.

800 **(F)** Images from Videos S7 and S8 showing INM events (arrows) in the otic vesicle after
801 nocodazole or vehicle (DMSO) treatment. H2B-GFP (green) and RFP-F (red) are shown.
802 Time is indicated relative to drug addition. The arrowhead marks a cell arrested in M
803 phase from the beginning of imaging. Scale bar, 20 μm.

804 **(G)** Quantification of INM events during a 206-min window, starting 30 min after drug
805 addition. Data from three embryos per condition. Student's *t*-test.

806 **(H)** Images from Videos S9 and S10 showing INM events (arrows) in the otic vesicle. RFP
807 or RFP-p50 was overexpressed under the hsp70 promoter (red). H2B-GFP was
808 expressed to label chromatin (green). Each number represents an INM event in RFP-
809 positive cells. Scale bar, 20 μm.
810 **(I)** Quantification of INM frequency over 300 min of imaging. Data from three embryos per
811 condition. Student's *t*-test. Scale bar, 20 μm.
812
813 **Figure 6. Nuclear migration is essential for M phase onset.**
814 **(A)** Sections of epididymal epithelium stained for γ-tubulin (green), pH3 (red), and DAPI
815 (blue). Centrosomes (arrowheads) localize near the apical surface during nuclear
816 migration, while centrioles move to opposite sides of the nucleus (arrows) only after it
817 reaches the apical side.
818 **(B)** Frames from Video S6. Nuclei labeled with H2B-RFP (red) and stable microtubules
819 labeled with EMTB-GFP (green) show MTOC/centrosomes (arrowheads) migrating to
820 opposite sides of the nucleus (arrows) after apical migration to form the spindle.
821 **(C)** Sections of epididymal epithelium stained for cyclin B1 (red), pH3 (green), and DAPI
822 (blue). Scale bar, 20 μm.
823 **(D)** Quantification for images shown in (C). Subcellular localization of Cyclin B1 grouped
824 by position of nuclei in the basal, middle and apical parts of the cell. Blue = cytoplasmic,
825 red = nuclear Cyclin B1 expression. n = 299 cells from three mice.
826
827 **Fig. 7. Summary of INM and cell division in simple columnar epithelium.**
828 A schematic summarizing apically directed INM, which is driven by dynein in late G2.
829 During prometaphase, actomyosin mediates mitotic rounding by constricting the
830 basolateral membrane, while lateral adhesions to neighboring interphase cells are
831 strengthened. Mitotic cells maintain attachment to the basal lamina during planar division.

832 **Supplemental Information**

833

834 **Legends for supplemental Videos**

835 **Video S1. Nuclear migration and mitosis in zebrafish otic vesicle.** Fertilized embryos
836 were microinjected with *in vitro* transcribed mRNA to express H2B-GFP, labeling
837 chromatin. Imaging of the otic vesicle began at approximately 22 hpf and continued for
838 170 minutes at 2-minute intervals.

839

840 **Video S2. Morphological changes of a mitotic cell in the zebrafish otic vesicle.** H2B-
841 GFP (green) labels chromatin, while RFP-F (red or gray) labels the plasma membrane.
842 The arrow highlights the nucleus, and arrowheads indicate the lateral plasma membrane.

843

844 **Video S3. F-actin dynamics in a mitotic cell of the zebrafish otic vesicle.** H2B-RFP
845 (red) labels chromatin, and GFP-hUtCH (green or gray) labels F-actin. The arrow marks
846 the nucleus, while arrowheads point to the lateral plasma membrane.

847

848 **Video S4. Nuclear migration and mitosis in the zebrafish otic vesicle following**
849 **DMSO treatment.** Embryos were microinjected with mRNA to express H2B-RFP (red)
850 and GFP-hUtrCH (green). Imaging started approximately 20 minutes after DMSO was
851 added at 22 hpf.

852

853 **Video S5. Nuclear migration and mitosis in the zebrafish otic vesicle following**
854 **Blebbistatin treatment.** Embryos were microinjected with mRNA to express H2B-RFP
855 (red) and GFP-hUtrCH (green). Imaging began approximately 25 minutes after
856 Blebbistatin was added at 22 hpf.

857

858 **Video S6. Microtubule dynamics in an otic vesicle cell entering the cell cycle.** H2B-

859 RFP (red) labels chromatin, and EMTB-GFP (green) labels stable microtubules.

860

861 **Video S7. Control otic vesicle treated with DMSO.** Embryos were microinjected with
862 mRNA to express H2B-GFP (green) and RFP-F (red). Imaging commenced
863 approximately 30 minutes after DMSO was added at 22 hpf.

864

865 **Video S8. Otic vesicle morphology following nocodazole treatment.** Embryos were
866 microinjected with mRNA to express H2B-GFP (green) and RFP-F (red). Imaging started
867 approximately 30 minutes after nocodazole was added at 22 hpf.

868

869 **Video S9. A control otic vesicle overexpressing RFP**. The zebrafish embryo was
870 microinjected with both mRNA to express H2B-GFP (green) and a plasmid to overexpress
871 RFP (red) in a heat shock-inducible manner. The heat shock treatment was performed at
872 20 hpf for 1hr. The otic vesicle was imaged at 1.5 hr after the heat shock was done.

873

874 **Video 10. A representative otic vesicle overexpressing RFP-p50**. The zebrafish
875 embryo was microinjected with both mRNA to express H2B-GFP (green) and a plasmid
876 to overexpress RFP-p50 (red) in a heat shock-inducible manner. The heat shock
877 treatment was performed at 20 hpf for 1hr. The otic vesicle was imaged at 1.5 hr after the
878 heat shock was done.

Fig.1

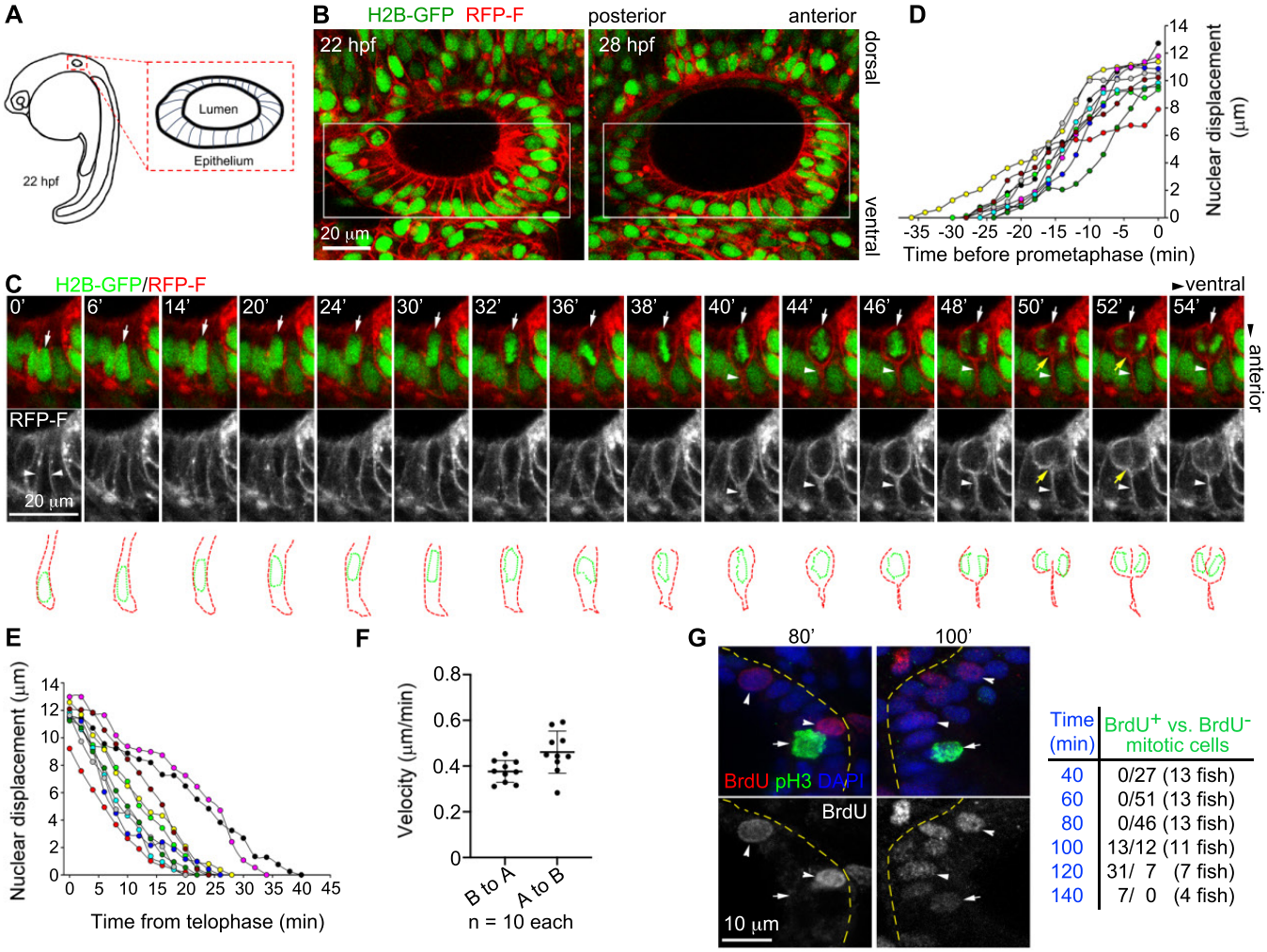

Time (min)	BrdU⁺ vs. BrdU⁻ mitotic cells
40	0/27 (13 fish)
60	0/51 (13 fish)
80	0/46 (13 fish)
100	13/12 (11 fish)
120	31/ 7 (7 fish)
140	7/ 0 (4 fish)

Figure 1. INM in zebrafish otic vesicle epithelium begins in late G2.

(A) Schematic of the zebrafish otic vesicle at approximately 22 hpf.

(B) Morphology of the otic vesicle epithelium at 22 hpf and 28 hpf. Embryos were microinjected with mRNA to express H2B-GFP (chromatin, green) and RFP-F (cell membrane, red). The boxed regions indicate areas used for INM analyses. Scale bar, 20 μm.

(C) Selected frames from Video S2. H2B-GFP (green) and RFP-F (red) label chromatin and the plasma membrane, respectively. Single-channel images of RFP-F are shown in the middle. White arrows indicate the nucleus or chromosomes of the tracked cell, white arrowheads highlight its basal protrusion and plasma membrane, and yellow arrows denote the cleavage furrow. The cell boundary and nucleolus of the tracked cell are outlined below. Scale bar, 20 μm.

(D, E) Nuclear trajectories before prometaphase (D) and after telophase (E). For daughter nuclei, only one that could be clearly tracked was analyzed.

(F) Velocity of pooled nuclear movements.

(G) Estimation of G2 length. Embryos at 24 hpf were labeled with BrdU, fixed at the indicated time points, and stained to visualize BrdU (red), pH3 (green), and DAPI (blue). Representative S-phase cells (arrowheads) and mitotic cells (pH3-positive, arrows) are shown. Yellow dashed lines indicate the basal membrane. Scale bar, 10 μm.

Fig. 2

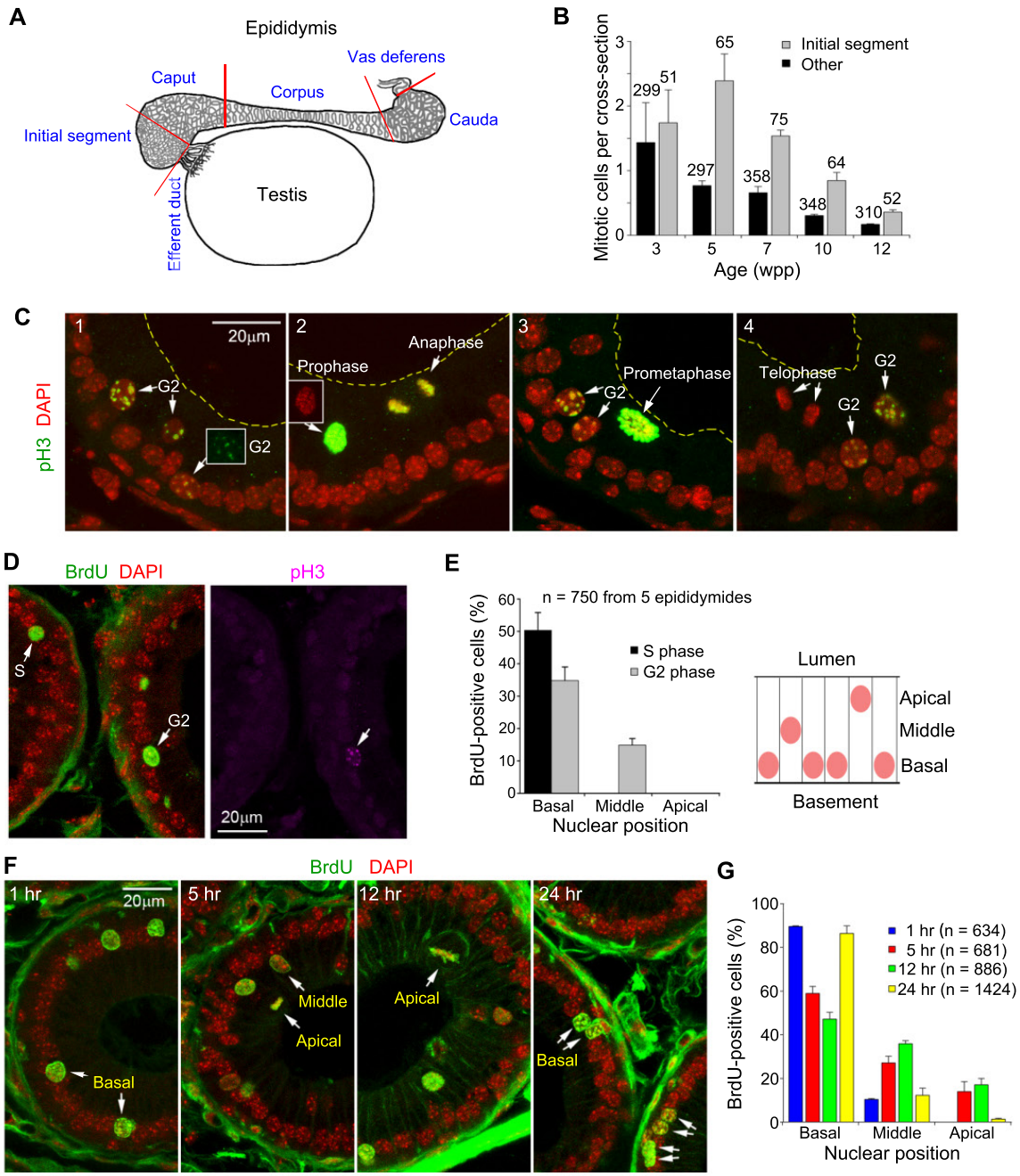

Figure 2. INM in the mouse epididymis resembles that in the zebrafish otic vesicle.

(A) Schematic of the anatomical structure of the mouse epididymis.

(B) Quantification of mitotic events per epididymal tubular cross-section. Mitotic cells were identified based on chromosome morphology and/or strong pH3 staining (see C). The number of analyzed tubular cross-sections is indicated above each histogram.

(C) Section images showing nuclear positioning at different cell cycle stages. Insets display pH3 (green) or DAPI (red) staining of the indicated nuclei. Yellow lines mark the apical surface. Scale bar, 20 µm.

(D, E) Section images and quantification (E) showing S-phase and G2-phase nuclei 1 hour after BrdU labeling. Scale bar, 20 µm.

(F, G) Section images and quantification showing the distribution of BrdU-positive nuclei or chromosome clusters at the indicated time points. Arrows in (F) indicate representative nuclei or chromosome clusters. Scale bar, 20 µm.

Fig. 3

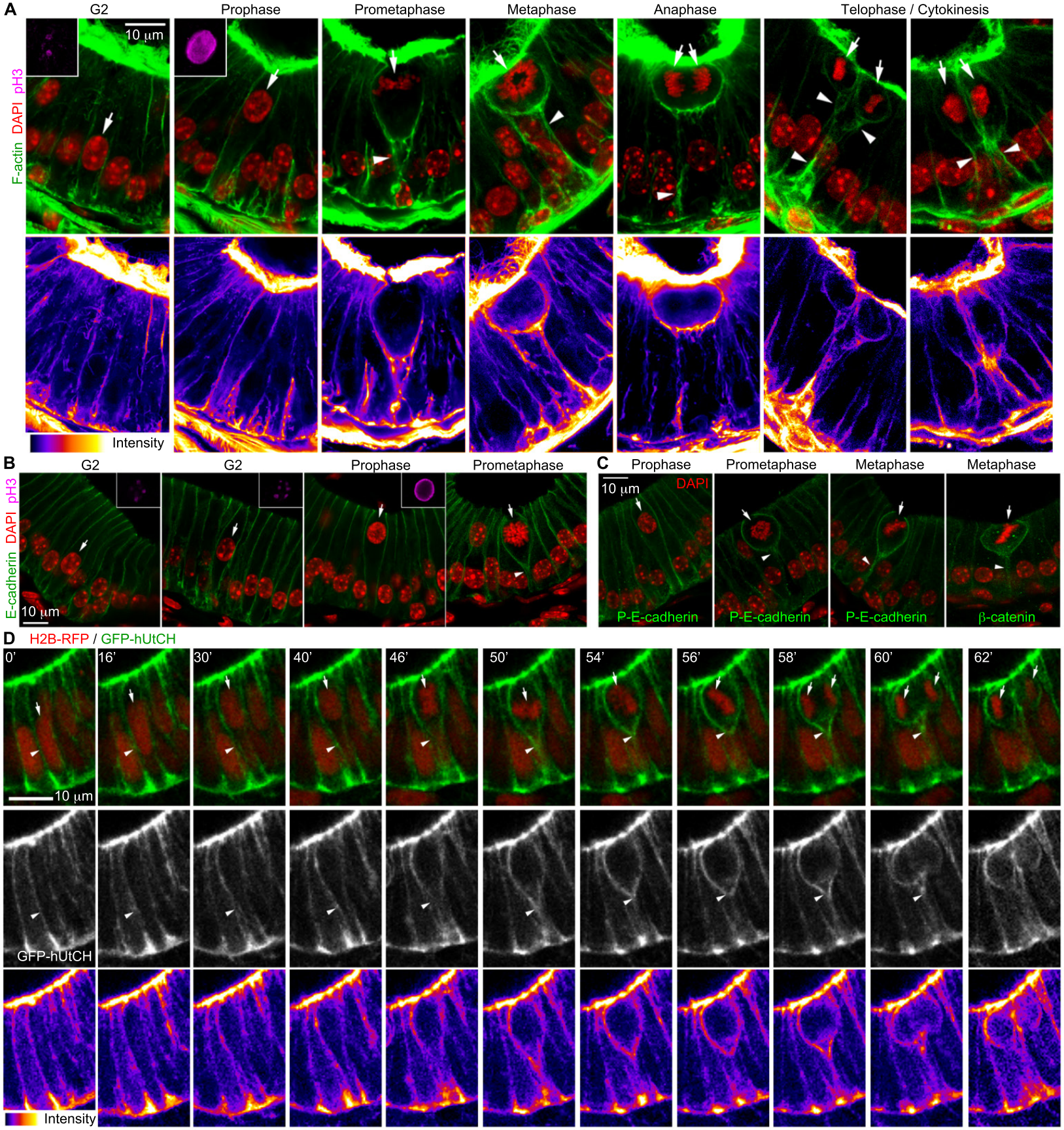

Figure 3. Cell shape dynamics and basal lamina attachment during INM and mitosis.

(A-C) Section images of mouse epididymis epithelium showing cell-cell interfaces labeled with the indicated markers (green). Insets show pH3 staining (magenta) in G2 or prophase cells. Arrows indicate G2 or M-phase cells, and arrowheads point to the narrow basal protrusions of mitotic cells. DAPI staining is shown in red. Fluorescent intensity of F-action signals in (A) is shown at the bottom. Scale bars, 10 µm.

(D) Selected frames from Video S3 showing GFP-hUtCH (green) and H2B-RFP (red). Single-channel GFP-hUtCH images are shown in grayscale at the bottom. Arrows indicate the nucleus or chromosomes of the tracked cell, while arrowheads highlight its basal process and plasma membrane. Fluorescent intensity of GFP signals is shown at the bottom. Scale bar, 10 µm.

Fig. 4

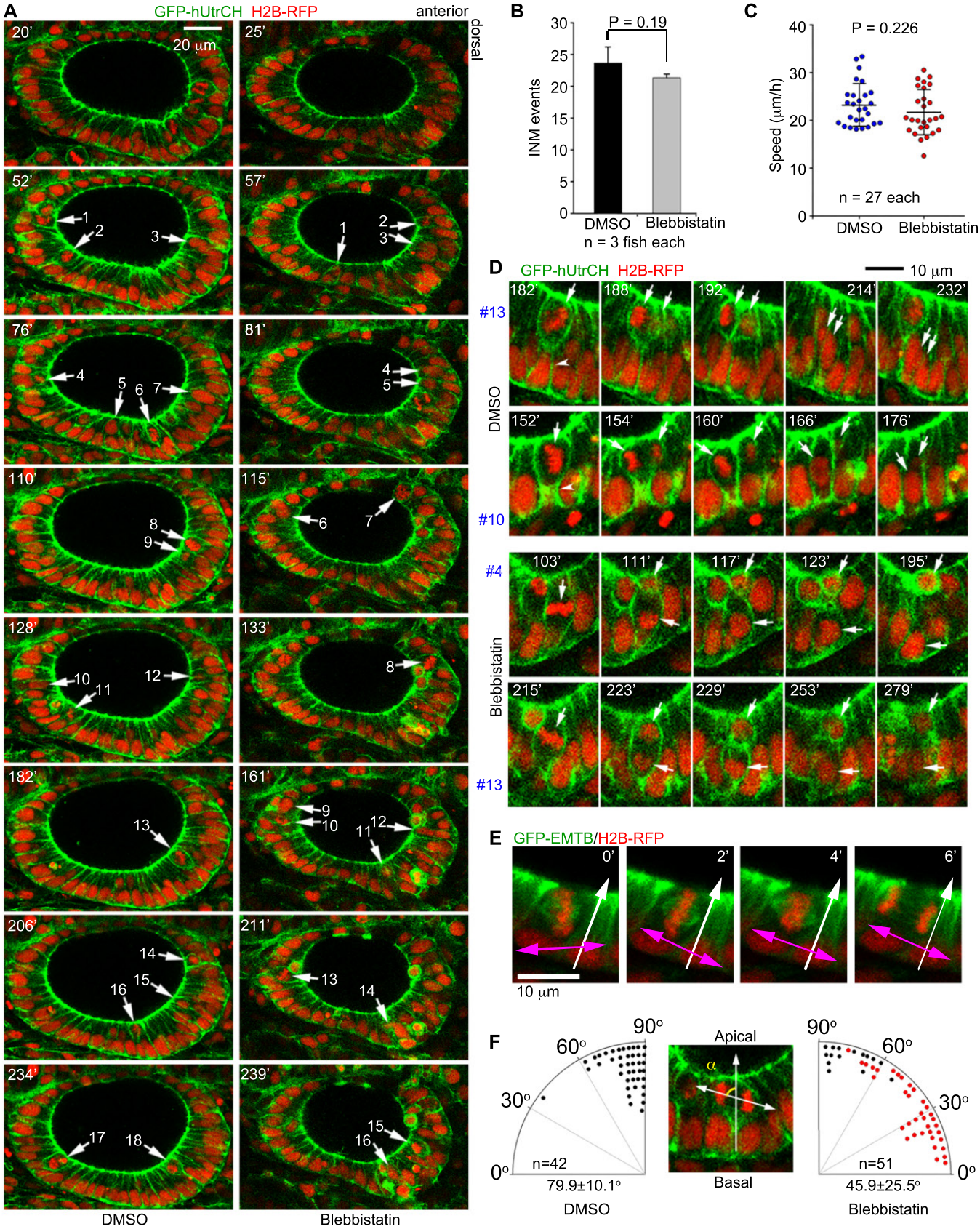

Figure 4. Myosin II activity regulates mitotic cell rounding, spindle orientation, and epithelial Integrity.
(A) Selected frames from Videos S4 and S5 showing INM events. H2B-RFP (red) and GFP-hUtrCH (green) are shown. Time is indicated relative to the addition of DMSO or blebbistatin. Each number represents a nuclear migration event and marks a mitotic cell. Scale bar, 20 µm. **(B)** Quantification of INM events during a 230-min window while epithelial cells remained columnar, starting 20 or 25 min after drug addition. Student's *t*-test. **(C)** Quantification of migration speed of pooled apically directed INM. Student's *t*-test. **(D)** Representative images from Videos S4 and S5 showing mitotic rounding, planar division, and daughter cell insertion after treatment. The locations of mitotic cells in the inner ear are indicated in (A) by the corresponding numbers. Arrows indicate parental or daughter nuclei. Scale bar, 10 µm. **(E)** Representative frames showing spindle orientation with GFP-EMTB (green) and H2B-RFP (red). Scale bar, 10 µm. **(F)** Statistical analysis of cell division angles. Each mitotic cell is represented as a dot in the radial histogram. Cells with apically retained daughter nuclei are highlighted in red.

Fig. 5

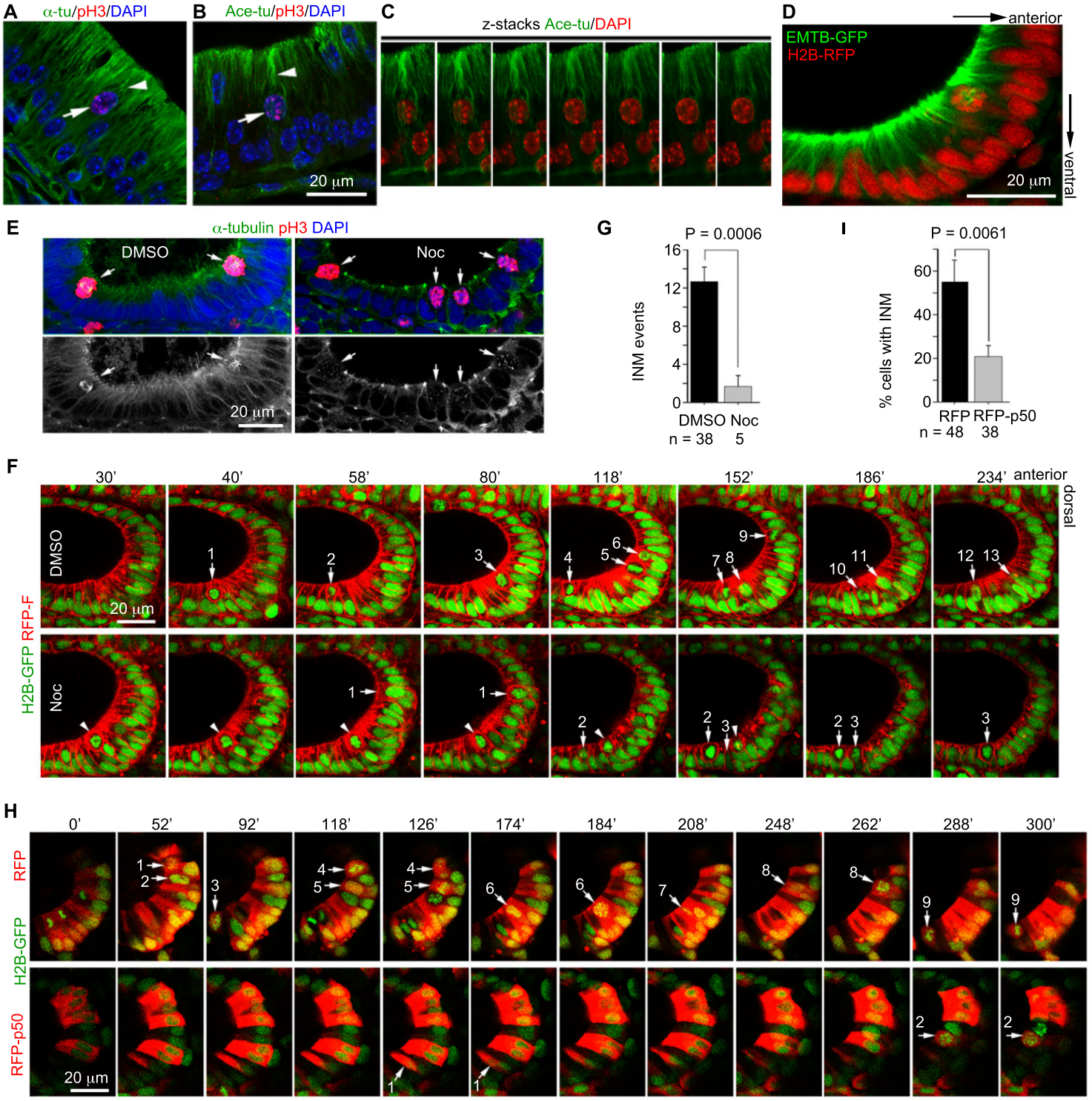

Figure 5. INM in zebrafish otic vesicle requires MTs and dynein. (A, B) Section images of epididymal epithelium stained for α-tubulin (A, green), acetylated tubulin (Ace-tu, B, green), pH3 (red), and DAPI (blue). Arrows indicate pH3+ cells, and arrowheads highlight microtubule bundles. Scale bars, 20 μm. **(C)** Z-stack images of the same cell as in (B), showing Ace-tu (green) and DAPI (red) staining. **(D)** Video frame showing EMTB-GFP (green) and H2B-RFP (red). Scale bar, 20 μm. **(E)** Nocodazole-induced microtubule disassembly. Zebrafish otic vesicle was stained for α-tubulin (green) and pH3 (red). DAPI (blue) staining is also shown. Single-channel α-tubulin images are displayed in grayscale at the bottom. Scale bar, 20 μm.
nocodazole or vehicle (DMSO) treatment. H2B-GFP (green) and RFP-F (red) are shown. Time is indicated relative to drug addition. The arrowhead marks a cell arrested in M phase from the beginning of imaging. Scale bar, 20 μm. **(G)** Quantification of INM events during a 206-min window, starting 30 min after drug addition. Data from three embryos per condition. Student's t-test. **(H)** Images from Videos S9 and S10 showing INM events (arrows) in the inner ear. RFP or RFP-p50 was overexpressed under the hsp70 promoter (red). H2B-GFP was expressed to label chromatin (green). Each number represents an INM event in RFP-positive cells. Scale bar, 20 μm. **(I)** Quantification of INM frequency over 300 min of imaging. Data from three embryos per condition. Student's *t*-test. Scale bar, 20 μm.

Fig. 6

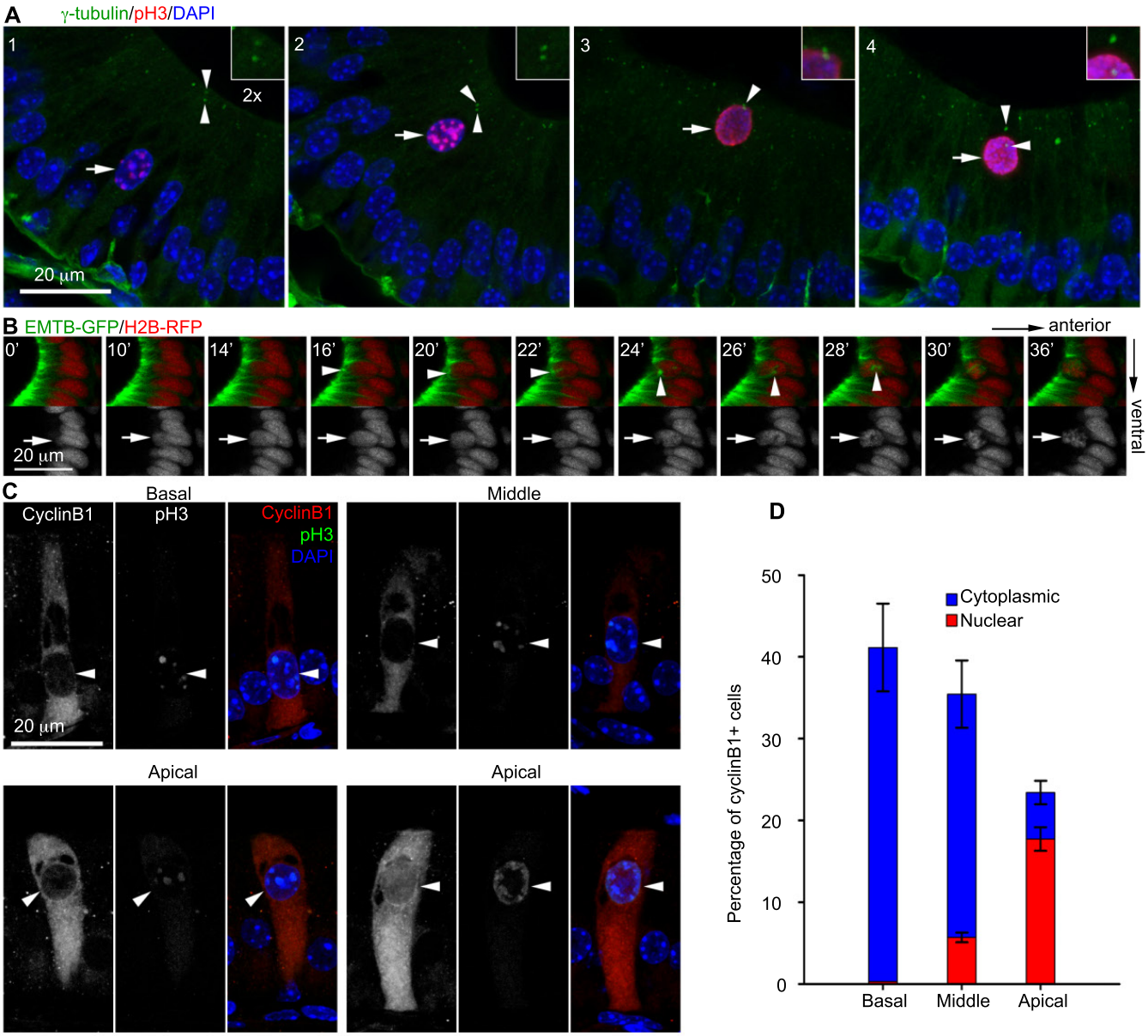

Figure 6. Nuclear migration is essential for M phase onset.

(A) Sections of epididymal epithelium stained for γ-tubulin (green), pH3 (red), and DAPI (blue). Centrosomes (arrowheads) localize near the apical surface during nuclear migration, while centrioles move to opposite sides of the nucleus (arrows) only after it reaches the apical side.

(B) Frames from Video S6. Nuclei labeled with H2B-RFP (red) and stable microtubules labeled with EMTB-GFP (green) show MTOC/centrosomes (arrowheads) migrating to opposite sides of the nucleus (arrows) after apical migration to form the spindle.

(C) Sections of epididymal epithelium stained for cyclin B1 (red), pH3 (green), and DAPI (blue). Scale bar, 20 μm.

(D) Quantification for images shown in (C). Subcellular localization of Cyclin B1 grouped by position of nuclei in the basal, middle and apical parts of the cell. Blue = cytoplasmic, red = nuclear Cyclin B1 expression. n = 299 cells from three mice.

Fig. 7

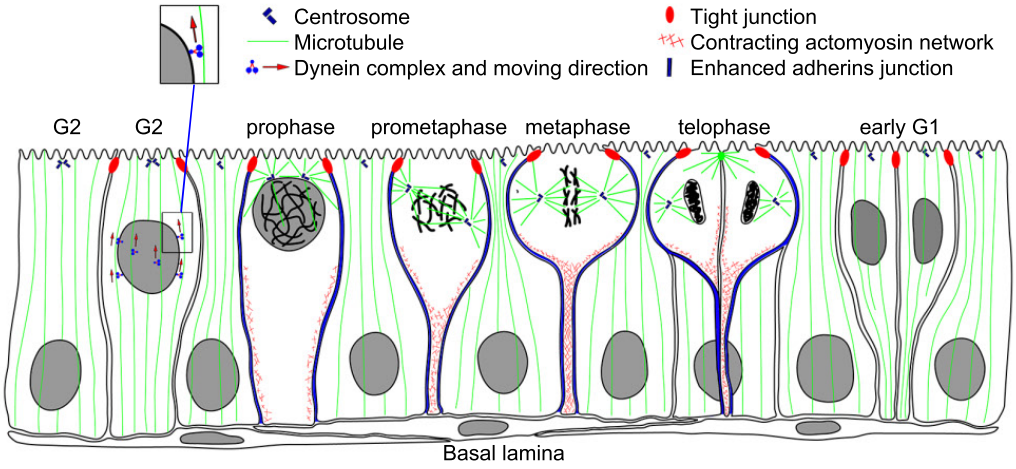

Figure 7. Summary of INM and cell division in simple columnar epithelium. A schematic summarizing apically directed INM, which is driven by dynein in late G2. During prometaphase, actomyosin mediates mitotic rounding by constricting the basolateral membrane, while lateral adhesions to neighboring interphase cells are strengthened. Mitotic cells maintain attachment to the basal lamina during planar division.